Transmission Line Rogowski Coil: Isolated Current Sensor With Bandwidth Exceeding 3 GHz for Wide-Bandgap Device

Yulei Wang, Teng Long, *Member, IEEE*, Mingrui Zou, Peng Sun, Jiakun Gong, Liang Wang,
Luke Shillaber, Frede Blaabjerg, *Fellow, IEEE*, Ke Jiang, *Senior Member, IEEE*,
and Zheng Zeng, *Member, IEEE*

***Abstract*—Rogowski coil (RC) has been commonly employed in power electronics due to its benefits of galvanic isolation, high-current measurement capability, and simple integration. However, the bandwidth of RC is restricted to tens of megahertz because of the inextricable resonance issue caused by its self-inductance and parasitic capacitance. This limitation hinders the ability of the RC to measure fast current transients such as those of wide-bandgap (WBG) power devices. In this letter, the concept of transmission line RC (TL-RC) is proposed to address the limitations of inductance and capacitance. The design criteria of double-ended impedance matching are further derived to ensure optimal signal integrity of TL-RC at gigahertz levels. These two concepts jointly form the isolated current sensor design with a bandwidth exceeding 3 GHz. Comparative experiments confirm the ultrafast and isolated advantages of the TL-RC for the WBG applications.**

***Index Terms*—Current sensor, transmission line Rogowski coil (TL-RC), ultrahigh bandwidth, wide-bandgap (WBG) device.**

I. Introduction

Current monitoring technology with high bandwidth and high integration is vital [1], [2], as it aligns with the high-density design goals in power electronics driven by the rapid switching speed of the wide-bandgap (WBG) device [3]. Recently, the Rogowski coil (RC) has attracted considerable attention due to its advantages in galvanic isolation, high-current measurement capability, and ease of integration [4]. However, as depicted in Fig. 1, the extremely fast switching speed of the WBG device approaches the theoretical limitation of current sensors. The ultrahigh bandwidth requirements for the measurement of SiC devices BW_{SiC}, which exceeds 100 MHz, and GaN devices BW_{GaN}, which exceeds 500 MHz [5], substantially surpass the bandwidth of commercial RCs, which is limited to just tens of megahertz (MHz) [6]. This poses a significant obstacle to the adoption of the RCs in WBG device current measurements, especially in the scenario of the ultrafast short-circuit (SC) and overcurrent protection for the GaN device [7], which exhibits a much lower SC withstanding time than its Si and SiC counterparts [8].

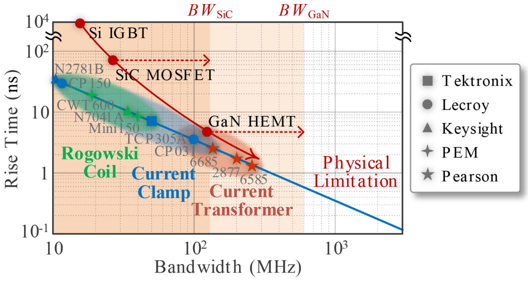

Fig. 1. State-of-the-art of isolated current sensors for the WBG device.

Numerous research efforts have been undertaken to promote the bandwidth of the RC from various aspects. Regarding the limitation, the conventional lumped-element model of the RC has been established, demonstrating that its bandwidth is primarily restricted to tens of MHz due to the resonance governed by self-inductance and parasitic capacitance [4]. Regarding the parasitic reduction, decreasing the number of turns is a simple approach for simultaneously lowering the self-inductance and parasitic capacitance, thereby increasing the resonant frequency [9]. Regarding the resonance compensation, the damping resistor is incorporated in order to mitigate the resonance [10] or to give the RC self-integration characteristics [11], [12]. In addition, the wave trap network is introduced at the output of the RC to offset the resonance [13] to further increase the bandwidth. These excellent contributions have driven the progress of the

---

Manuscript received 7 June 2023; revised 22 July 2023; accepted 13 August 2023. Date of publication 21 August 2023; date of current version 22 September 2023. This work was supported in part by the National Natural Science Foundation of China under Grant 52177169 and in part by the Chongqing Research Program of Basic Research and Frontier Technology under Grant cstc2022ycjh-bgzxm0155. *(Corresponding author: Zheng Zeng.)*

Yulei Wang, Mingrui Zou, Peng Sun, Jiakun Gong, Liang Wang, and Zheng Zeng are with the State Key Laboratory of Power Transmission Equipment and System Security and New Technology, Chongqing University, Chongqing 400044, China (e-mail: 18252116069@163.com; 928154685@qq.com; sunpeng_96@163.com; 1285646754@qq.com; wangliangedu@126.com; zengerzheng@126.com).

Teng Long and Luke Shillaber are with the Department of Engineering, University of Cambridge, CB3 0FA Cambridge, U.K. (e-mail: tl322@cam.ac.uk; ls669@cam.ac.uk).

Frede Blaabjerg is with the AAU Energy, Aalborg University, 9220 Aalborg, Denmark (e-mail: fbl@energy.aau.dk).

Ke Jiang is with the School of Integrated Circuits, Tsinghua University, Beijing 100084, China (e-mail: kejiang@nexperia.com).

Digital Object Identifier 10.1109/TPEL.2023.3306103

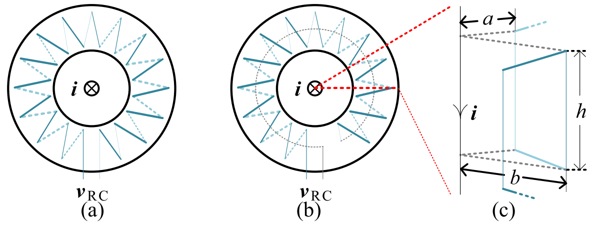

(a) (b) (c)

Fig. 2. Physical configuration of the traditional RC. (a) RC without a signal return path. (b) RC with a signal return path. (c) Cross section of a single-turn.

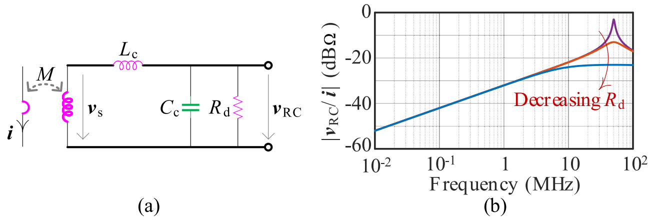

(a) (b)

Fig. 3. Model and characteristic of the traditional RC. (a) Lumped-element model. (b) Typical forward transfer characteristic.

high-bandwidth RC for the WBG applications. However, the resonance issue attributed to inductance and capacitance still remains. Moreover, the transmission line effect poses even more complex challenges to the signal integrity of the RC at higher frequencies ranging from hundreds of MHz to even gigahertz (GHz).

Driven by these challenges, the concept of transmission line RC (TL-RC) is proposed to break the double shackle on the bandwidth in the traditional RC. The design criteria of double-ended impedance matching are further introduced for optimal signal integrity. The rest of this letter is organized as follows. In Section II, two typical configurations of the traditional RC are analyzed to clarify the cause of bandwidth limitation. On this basis, the concept and typical configuration of the TL-RC are introduced, and its bandwidth extension mechanism is further explored to establish the essential design criteria of the double-ended impedance matching for the ultrafast RC. In Section III, the excellent performance of the developed TL-RC is examined by comprehensive experiments in the frequency and time domains. Finally, Section IV concludes this letter.

II. MODEL AND DESIGN OF ISOLATED CURRENT SENSOR WITH ULTRAHIGH BANDWIDTH FOR WBG DEVICE APPLICATION

A. *Typical Configuration of Traditional RC*

Multiple configurations of the traditional RC have been derived, and depending on the signal return path, these RCs can mainly be divided into two categories, as shown in Fig. 2(a) and (b), where $\boldsymbol{i}$ is the measured current at the circuit under test (CUT). $\boldsymbol{v}_{\mathrm{RC}}$ is the output voltage signal of the RC, and will be transmitted to subsequent circuits for integral operation.

The time-varying magnetic field generated by $\boldsymbol{i}$ is captured by the RC, and further induces the voltage signal $\boldsymbol{v}_{\mathrm{s}}$, which is uniformly distributed on the RC winding, expressed as

$$\boldsymbol{v}_{\mathrm{s}} = sM\boldsymbol{i} \tag{1}$$

where s is the differential operator. M is the mutual-inductance between the CUT and coil, which is determined by the physical dimension of the winding displayed in Fig. 2(c), written as

$$M = \frac{\mu_0}{2\pi} N h \ln \frac{b}{a} \tag{2}$$

where μ_0 is the vacuum permeability. N is the number of winding turns. h, a, and b are the height, inner radius, and outer radius of the coil, respectively. Equation (1) is considered accurate over the wideband range, which is the prerequisite for the wideband current measurement on the basis of the principle of the RC.

Induced $\boldsymbol{v}_{\mathrm{s}}$ then transmits through the entire RC structure and is finally applied on the load resistor to generate $\boldsymbol{v}_{\mathrm{RC}}$ that can be postprocessed by the subsequent circuits. Therefore, the forward transfer property, or bandwidth, of the RC is related to the parasitics resulting from the specific structure of the RC.

B. *Bandwidth Limitation of Traditional RC*

The lumped-element model of the traditional RC is illustrated in Fig. 3(a), from which the forward transfer characteristic of the RC can be derived as

$$\frac{\boldsymbol{v}_{\mathrm{RC}}}{\boldsymbol{i}} = sM\frac{\boldsymbol{v}_{\mathrm{RC}}}{\boldsymbol{v}_{\mathrm{s}}} = \frac{sMR_{\mathrm{d}}}{s^2 L_{\mathrm{c}} C_{\mathrm{c}} R_{\mathrm{d}} + sL_{\mathrm{c}} + R_{\mathrm{d}}} \tag{3}$$

where L_{c} is the lumped self-inductance of the RC depending on its winding structure, which can be modeled as

$$L_{\mathrm{c}} = \frac{\mu_0}{2\pi} N^2 h \ln \frac{b}{a}. \tag{4}$$

C_{c} represents the lumped capacitance of the RC, which is normally difficult to accurately determine through analytical calculation, due to the intricate and variable configuration of the RC. R_{d} is the damping resistor added to the output end of the traditional RC to control the resonance caused by L_{c} and C_{c}.

The typical forward transfer characteristics of the traditional RC are depicted in Fig. 3(b). It is evident that, despite the broadband induced $\boldsymbol{v}_{\mathrm{s}}$, the bandwidth of the traditional RC is limited to tens of MHz, as shown in Fig. 1, due to the combined obstacles of L_{c} and C_{c}. Although decreasing the number of winding turns to concurrently reduce L_{c} and C_{c} is a simple method for raising the resonant frequency [9], the issue of L_{c} and C_{c} constraining the broadband transmission of the induced $\boldsymbol{v}_{\mathrm{s}}$ to the end is unsolved.

C. *Concept Definition of Proposed TL-RC*

To surmount the dual constraints for high-frequency signal transmission on the winding in the traditional RC, the TL-RC concept is proposed. By providing a complete reference plane for the signal winding, this concept strives to integrate the structure for current induction with the transmission line configuration, thereby enabling the wideband transmission of the induced signals to the end.

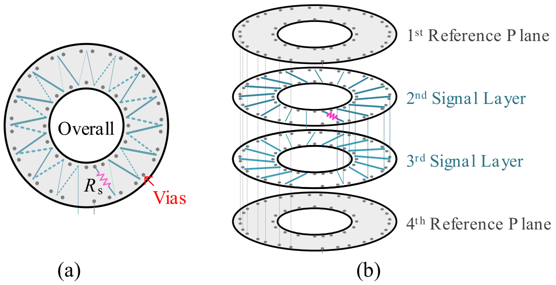

Fig. 4. Overall configuration of TL-RC. (a) Vertical view. (b) Multilayer layout.

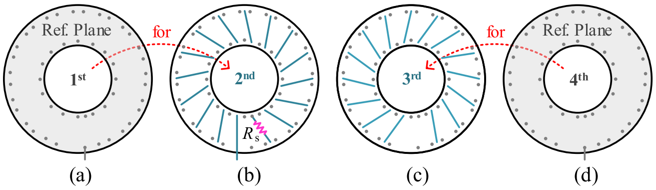

Fig. 5. Multilayer decomposition of TL-RC. (a) First reference layer. (b) Second signal layer. (c) Third signal layer. (d) Fourth reference layer.

The overall configuration of the proposed TL-RC is shown in Fig. 4. Its multilayer decomposition diagrams are depicted in Fig. 5(a)–(d). Two identical reference planes are added outside the signal winding, as explained in Fig. 4(b), where the first-layer plane in Fig. 5(a) provides a reference for the second-layer signal winding in Fig. 5(b). Similarly, the fourth-layer plane in Fig. 5(d) provides a reference for the third-layer winding in Fig. 5(c).

Source resistor R_s is added at the source end of the signal winding, instead of the direct SC in the traditional RC depicted in Fig. 2(b), for the purpose of the impedance matching. Moreover, vias connecting the first- and fourth-layer planes are important, and should be placed as close to the vias connecting the second- and third-layer signal winding as possible, for the purpose of the shortest signal return path.

D. Bandwidth Extension Mechanism of Proposed TL-RC

To achieve the working frequency of the RC stepping into hundreds of MHz or beyond, taking into account the inevitable high-frequency transmission line effect, the theoretical analysis and design deduction under the framework of the distributed-element model are essential. The distributed-element model transformation from the traditional RC to the proposed TL-RC is mainly divided into three steps, as explained in Fig. 6.

The distributed-element model of the traditional RC is shown in Fig. 6(a) and (b), where M_0 is the distributed mutual-inductance between the CUT and the coil. L_{c0} is the equivalent winding self-inductance in the distributed mode. C_{cn} ($n = 1, 2, \ldots$) represents the distributed parasitic capacitance, where n refers to the discontinuity of capacitance along the signal winding due to the lack of a complete reference plane in the traditional RC. $\boldsymbol{v}_0 = sM_0\boldsymbol{i}$ is the distributed induced voltage. 50 Ω represents a unified input impedance of 50 Ω for the subsequent signal-receiving and processing circuits.

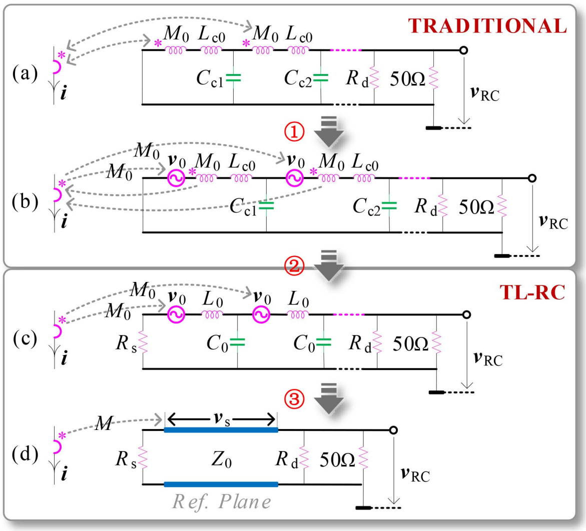

Fig. 6. Distributed-element model transformation from the traditional RC to TL-RC.

The distributed-element model of the TL-RC is shown in Fig. 6(c) and (d), where L_0 and C_0 are the distributed inductance and capacitance between the signal winding and its corresponding reference plane, respectively. $Z_0 = \sqrt{L_0/C_0}$ is the characteristic impedance of the transmission line structure of the TL-RC.

Step ①: The effects of M_0 between the CUT and the coil in Fig. 6(a) are separated into two parts. M_0 directed from the CUT toward the coil generates $\boldsymbol{v}_0$ due to $\boldsymbol{i}$, while M_0 directed from the coil toward the CUT causes interference to the CUT when $\boldsymbol{v}_0$ travels along the winding, as shown in Fig. 6(b).

Step ②: After adding a complete reference (or return) plane, the distributed-element model of the traditional RC in Fig. 6(b) is transformed to that of the TL-RC in Fig. 6(c).

The return of any signal will attempt to transmit along the path with the least impedance, which is dominated by the loop inductance at high frequency. As a result, the high-frequency signal tends to return via the mirror path of the outgoing signal, as it creates the smallest possible loop area with the lowest inductance [14]. The TL-RC concept provides a complete return plane for the transmission of the induced signals, allowing high-speed return signals to automatically locate their own path with the smallest loop area (lowest inductance), as shown in Fig. 7(b).

At this stage, the outgoing signal current at any location on the winding is the same in magnitude but opposite in direction to the return current on the reference plane. This causes the central magnetic field of the coil to cancel out. Thus, there will be an equivalent magnetic field-free region inside the winding, equivalent to the coil that does not exhibit the self-induction effect, meaning that the transmission of $\boldsymbol{v}_0$ is no longer affected by L_{c0}. Similarly, due to the mirror return effect, there will be no change in the magnetic field surrounding the CUT during $\boldsymbol{v}_0$ transmission; M_0 from the coil to CUT can thus be ignored.

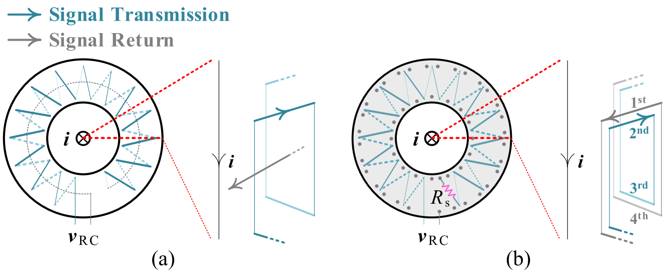

Fig. 7. Signal return path at the high frequency of (a) traditional RC and (b) TL-RC.

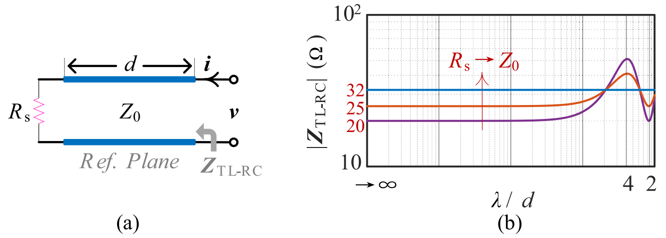

Fig. 8. Characteristic impedance calculation of TL-RC. (a) Equivalent circuit model. (b) Input impedance of TL-RC with fixed Z_0 and varied R_s.

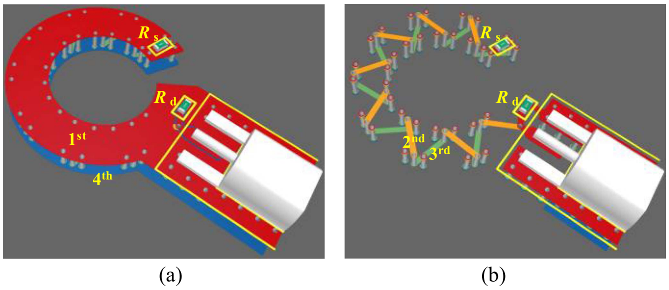

Fig. 9. Layout of the proposed TL-RC. (a) First and fourth reference layers. (b) Second and third signal layers.

L_{c0} and M_0 will finally be replaced by L_0, as shown in Fig. 6(c). C_{cn}, which is discontinuous and difficult to quantify, will also be replaced by C_0, which can be designed quantitatively due to the tight coupling between the winding and the reference plane. It must be emphasized that not only do L_0 and C_0 not hinder the signal transmission, but rather become essential conditions for the electromagnetic energy conversion during $\boldsymbol{v}_0$ propagation. This effectively breaks the double restrictions of L_c and C_c in the traditional RC.

***Step* ③:** The distributed-element model in Fig. 6(c) can be further simplified to the transmission line model in Fig. 6(d), which is just the concept of the proposed TL-RC. It is noted that the induced $\boldsymbol{v}_s$, distributed linearly over the entire transmission line, will propagate simultaneously in both directions toward the source end R_s and the load end R_d of the coil. To avoid any signal distortion and bandwidth reduction due to the internal signal reflection, the TL-RC design must satisfy the condition of the double-ended impedance matching, which is expressed as

$$R_s = Z_0 = R_d || 50. \tag{5}$$

At this point, R_d no longer undertakes the traditional role of suppressing resonance caused by L_c and C_c, but rather being adjusted for the output impedance matching of the TL-RC.

Serious issues, such as high-frequency impedance distortion and bandwidth reduction, related to the internal signal reflection caused by the impedance mismatching in high-speed measurement can be found in [5] and [15], and are given a brief explanation in Section II-E.

E. Characteristic Impedance Calculation of Proposed TL-RC

Based on Figs. 4(a) and 6(d), the transmission line model of the TL-RC is shown in Fig. 8(a), where d is the total length of the signal winding. According to the transmission line theory, the input impedance of the TL-RC $\boldsymbol{Z}_{\text{TL-RC}}$ is calculated by [15]

$$\boldsymbol{Z}_{\text{TL}-\text{RC}}(\lambda) = \frac{\boldsymbol{v}}{\boldsymbol{i}} = Z_0 \frac{R_s + \text{j}Z_0 \tan(2\pi d/\lambda)}{Z_0 + \text{j}R_s \tan(2\pi d/\lambda)} \tag{6}$$

where λ is the wavelength of input signals. $|\boldsymbol{Z}_{\text{TL-RC}}|$ under the condition of the fixed $Z_0 = 32\ \Omega$ and varied R_s (20 Ω, 25 Ω, and 32 Ω) is calculated according to (6), as depicted in Fig. 8(b).

It can be observed that, due to the impedance mismatching, or $R_s \neq Z_0$, the $|\boldsymbol{Z}_{\text{TL-RC}}|$ witnesses remarkable distortion at high frequencies, but as R_s gradually approaches Z_0 to finally realize impedance matching, or $R_s = Z_0$, the high-frequency fluctuation of the $|\boldsymbol{Z}_{\text{TL-RC}}|$ significantly decreases, $|\boldsymbol{Z}_{\text{TL-RC}}|$ exhibits near-pure resistance characteristics over a wide range of frequencies [5]. In this case, the induced signals can be loaded onto the load resistor completely with negligible distortion, thereby realizing the highest system bandwidth performance.

As the signal frequency increases, λ/d decreases gradually, and when $\lambda = 4d$

$$\boldsymbol{Z}_{\text{TL}-\text{RC}}(\lambda = 4d) = Z_0 \frac{R_s + \text{j}Z_0 \tan[2\pi d/(4d)]}{Z_0 + \text{j}R_s \tan[2\pi d/(4d)]} = \frac{Z_0^2}{R_s}. \tag{7}$$

Since $\boldsymbol{Z}_{\text{TL-RC}}$ can be accurately measured with a vector network analyzer (VNA), and R_s can be set to a random nonzero value just for the initial calculation, Z_0 is thus obtained by

$$Z_0 = \sqrt{|\boldsymbol{Z}_{\text{TL}-\text{RC}}(\lambda = 4d)|\, R_s}. \tag{8}$$

According to (5) and (8), the target values of R_s and R_d can be finally confirmed.

III. EXPERIMENTAL VALIDATIONS AND ANALYSES

A. Design Parameters of TL-RC

The prototype based on the TL-RC concept is developed, as presented in Fig. 9. Detailed design parameters of the prototype are listed in Table I.

To accurately calibrate Z_0 for the developed prototype, R_d is not welded at first, while R_s of 20 Ω is welded onto the PCB for the initial measurement and calculation. The input impedance of the developed TL-RC prototype is then measured by the VNA Agilent E5061B, as shown in Fig. 10(a). It can be seen that

TABLE I
DESIGN PARAMETERS OF TL-RC PROTOTYPE

Parameters	Value	Parameters	Value
Turn number (N)	8	Mutual inductance (M)	0.75 nH
Coil height (h)	1.16 mm	Wave impedance (Z_0)	32 Ω
Inner radius (a)	4 mm	Source resistor (R_s)	32 Ω
Outer radius (b)	6 mm	Load resistor (R_d)	89 Ω

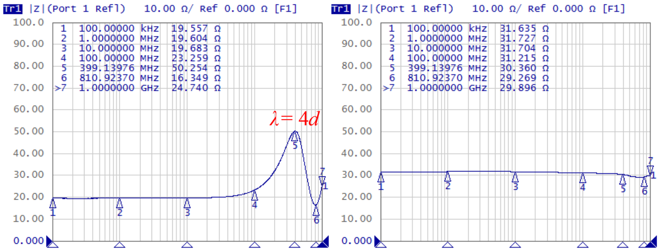

(a) (b)

Fig. 10. Input impedance (100 kHz–1 GHz) of the proposed TL-RC under different R_s. (a) $R_s = 20\ \Omega$. (b) $R_s = 32\ \Omega$.

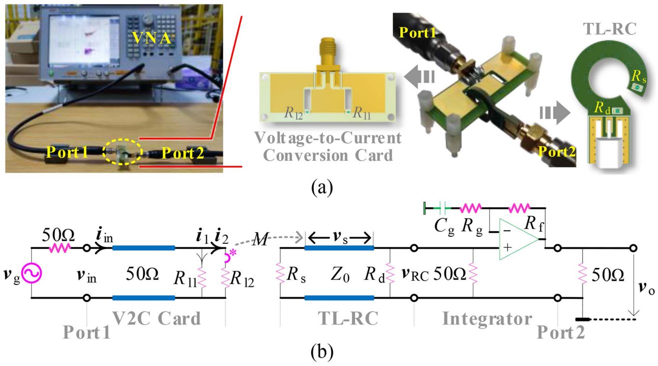

(a)

(b)

Fig. 11. Bandwidth calibration of TL-RC. (a) Test rig. (b) Equivalent circuit model.

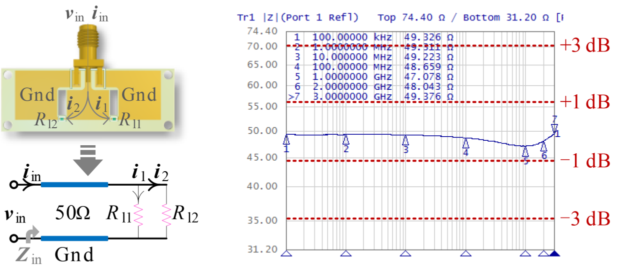

(a) (b)

Fig. 12. V2C card. (a) Equivalent circuit model. (b) Input impedance.

$f = 399$ MHz at frequency marker 5 marks the frequency where $\lambda = 4d$; at this point, $|\boldsymbol{Z}_{\text{TL-RC}}(\lambda = 4d)| = 50\ \Omega$. According to (8), Z_0 can be further calculated to have a value of 32 Ω. On the basis that $Z_0 = 32\ \Omega$, and following (5), the values of R_s and R_d are finally determined to be 32 Ω and 89 Ω, respectively, as concluded in Table I.

After welding an $R_s = 32\ \Omega$ to the TL-RC prototype, its input impedance is also measured, as displayed in Fig. 10(b). It can be seen that the fluctuation ranges of the input impedance of TL-RC witness a significant decrease from 8 dB at $R_s = 20\ \Omega$ to just within 1 dB at $R_s = 32\ \Omega$, further proving the correctness of the calibration value of Z_0.

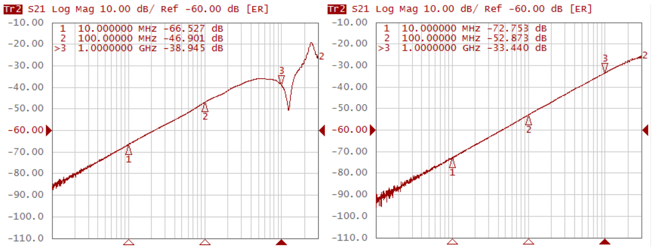

(a) (b)

Fig. 13. Frequency characteristics (1 MHz–3 GHz) of TL-RC under $Z_0 = R_d \parallel 50$ and varied R_s. (a) $R_s = 0\ \Omega$. (b) $R_s = Z_0$.

B. *Bandwidth Calibration of TL-RC*

To calibrate the frequency properties of the developed TL-RC, the forward transmission coefficient $\boldsymbol{S}_{21}$ is measured by the VNA E5061B.

To achieve precise, broadband, and high-frequency current signals, a voltage-to-current (V2C) conversion card utilizing the coplanar waveguide principle with 50 Ω characteristic impedance is developed, as depicted in Fig. 12(a). The load resistors R_{11} and R_{12} are both set to 100 Ω. TL-RC can be inserted into the slots of V2C card to measure current signals, as indicated in Fig. 11(a).

The input impedance of the V2C card $|\boldsymbol{Z}_{in}|$ is measured with VNA, as shown in Fig. 12(b). It can be observed that $|\boldsymbol{Z}_{in}|$ fluctuates within ±1 dB over a frequency range of 3 GHz, guaranteeing a precise bandwidth calibration of the TL-RC.

Generally, traditional RC exhibits impedance mismatching at both ends, taking the most-overlooked mismatching at the source end ($R_s = 0\ \Omega$) as an example, while the load end is always kept matching ($Z_0 = R_d \parallel 50$). Fig. 13 presents the measured results indicating that a dip distortion near 1.2 GHz in Fig. 13(a) is mainly due to the strong signal reflection at the source end. However, after fulfilling the double-ended matching condition, the bandwidth of TL-RC experiences a significant increase from 470 MHz to over 3 GHz, as shown in Fig. 13(b).

Benefiting from the natural open-loop integral properties of amplifiers over a very wide range of frequencies, as shown in Fig. 14, the wideband active integrator is developed to compensate for the differential characteristics of the TL-RC. The principle of the integrator is explained in Fig. 11(b), where

$$20\lg\left[1 + R_f \bigg/ \left(R_g + \frac{1}{2\pi f C_g}\right)\right] > \max\left[A_{OL}\ (\text{dB})\right] \quad (9)$$

with $\max[A_{OL}(\text{dB})]$ representing the maximum value of the open-loop characteristics of amplifiers. For the employed high-speed amplifier TI OPA859 [16], the $\max[A_{OL}(\text{dB})]$ is 65 dB, as shown in Fig. 14. C_g is added to set the dc gain to 1, to prevent potential dc saturation due to the excessive dc gain.

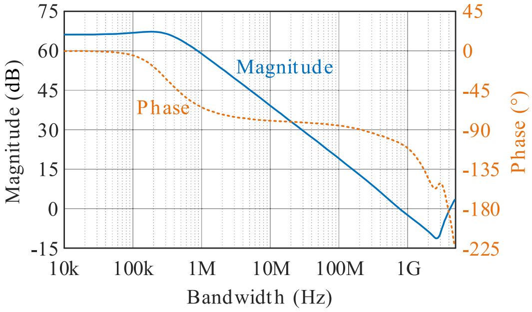

Fig. 14. Open-loop characteristics (10 kHz–5 GHz) of OPA859 [16].

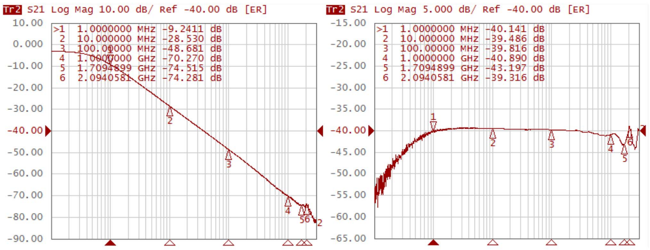

(a) (b)

Fig. 15. Frequency characteristics (100 kHz–3 GHz) of (a) integrator with a 60 dB attenuator and (b) TL-RC with integrator.

TABLE II
CURRENT SENSORS FOR EVALUATION AND COMPARISON

Current Sensor	Principle	Isolation	Bandwidth	Inductance
SDN-414-025	Current shunt	×	0.5 GHz	3.61 nH
IM-Shunt [5]	Current shunt	×	>3.0 GHz	<0.1 nH
TL-RC	Rogowski coil	√	>3.0 GHz	N/A*

*Insertion inductance of TL-RC is related to the specific configuration of CUT.

Fig. 15(a) displays the $|S_{21}|$ of the integrator with a 60 dB attenuator, which fits well with the open-loop properties of the OPA859 in Fig. 14. An attenuator is necessary, due to the input damage level of +20 dBm of the VNA E5061B, to avoid the potential damage to VNA. The $|S_{21}|$ of the TL-RC incorporating the integrator is presented in Fig. 15(b). Owing to the wideband TL-RC and integrator, the system exhibits a very flat frequency response from 1 MHz to over 1 GHz. A spike distortion observed near 2.09 GHz can be attributed mainly to the inadequate open-loop phase margin of the OPA859 being used, as shown in Fig. 14.

C. Comprehensive Performance Verification Based on DPT

The developed TL-RC is evaluated and compared with the state-of-the-art current shunts listed in Table II using the GaN HEMT-based double pulse test (DPT) rig, as shown in Fig. 16. The oscilloscope Lecroy 715Zi (1.5 GHz/20 GS/s) and GaN E-HEMT GS66508B (650 V/30 A) are employed, and experimental results are described in Fig. 17. Note that a wide gold-plated copper piece shown in Fig. 16(a) is used to short current testing points for isolated current measurement, in order to minimize the insertion inductance of the TL-RC to CUT.

(a) (b)

Fig. 16. Configuration of (a) DPT test rig and (b) TL-RC prototype.

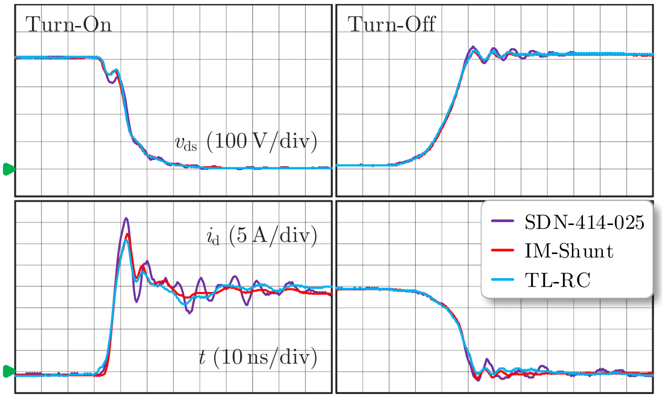

Fig. 17. Measured switching trajectories by using proposed TL-RC.

As seen in Fig. 17, benefitting from the ultrahigh bandwidth of the developed TL-RC, i_{d} waveform specifics captured by the TL-RC closely resemble those acquired by the IM-shunt that has a bandwidth above 3 GHz, as opposed to the current overshooting and ringing observed by the commercial shunt SDN-414-025, which has a huge insertion inductance and the resulting low measurement bandwidth of only 500 MHz [5].

However, low-frequency oscillations are still observed during switching transitions measured by the TL-RC. This may be due to the absence of low-frequency measurement capabilities, which can be addressed using a simple RC passive network [4]. Further elaboration on this method will not be given in detail.

IV. CONCLUSION

In this letter, novel concepts of TL-RC and double-ended impedance matching are proposed for ultrafast isolated current measurement in WBG applications. The bandwidth of the traditional RC is blocked simultaneously by L_{c} and C_{c}, but this can be effectively broken by employing the TL-RC configuration that provides a complete reference for the signal winding. At this point, the bandwidth is just determined by whether the double-ended matching condition is satisfied, and once satisfied, an isolated current sensor with the bandwidth exceeding 3 GHz can be realized. Comparative experiments further ensure ultrafast and isolated advantages of the TL-RC for the emerging WBG applications.

REFERENCES

[1] A. Rafiq and S. Pramanick, “Ultrafast protection of discrete SiC MOSFETs with PCB coil-based current sensors,” *IEEE Trans. Power Electron.*, vol. 38, no. 2, pp. 1860–1870, Feb. 2023.

[2] J. Wang, S. Mocevic, R. Burgos, and D. Boroyevich, “High-scalability enhanced gate drivers for SiC MOSFET modules with transient immunity beyond 100 V/ns,” *IEEE Trans. Power Electron.*, vol. 35, no. 10, pp. 10180–10199, Oct. 2020.

[3] J. W. Kolar et al., “Application of WBG power devices in future 3-Φ variable speed drive inverter systems ’How to handle a double-edged sword’,” in *Proc. IEEE Int. Electron Devices Meeting*, 2020, pp. 597–600.

[4] Y. Shi, Z. Xin, P. C. Loh, and F. Blaabjerg, “A review of traditional helical to recent miniaturized printed circuit board Rogowski coils for power-electronic applications,” *IEEE Trans. Power Electron.*, vol. 35, no. 11, pp. 12207–12222, Nov. 2020.

[5] Y. Wang, Z. Zeng, T. Long, P. Sun, L. Wang, and M. Zou, “Impedance-matching shunt: Current sensor with ultrahigh bandwidth and extremely low parasitics for wide-bandgap device,” *IEEE Trans. Power Electron.*, vol. 37, no. 10, pp. 11528–11533, Oct. 2022.

[6] Power Electronics Measurement, “CWT current probe,” 2020. [Online]. Available: https://www.pemuk.com/products/cwt-current-probe.aspx

[7] W. L. Jiang et al., “An integrated GaN overcurrent protection circuit for power HEMTs using SenseHEMT,” *IEEE Trans. Power Electron.*, vol. 37, no. 8, pp. 9314–9324, Aug. 2022.

[8] X. Lyu et al., “A reliable ultrafast short-circuit protection method for E-mode GaN HEMT,” *IEEE Trans. Power Electron.*, vol. 35, no. 9, pp. 8926–8933, Sep. 2020.

[9] K. Wang, X. Yang, H. Li, L. Wang, and P. Jain, “A high-bandwidth integrated current measurement for detecting switching current of fast GaN devices,” *IEEE Trans. Power Electron.*, vol. 33, no. 7, pp. 6199–6210, Jul. 2018.

[10] A. P. Sirat, H. Niakan, C. Roy, and B. Parkhideh, “Rogowski-pair sensor for high-speed switch current measurements without reset requirement,” in *Proc. IEEE Energy Convers. Congr. Expo.*, 2022, pp. 1–8.

[11] V. Dubickas and H. Edin, “High-frequency model of the Rogowski coil with a small number of turns,” *IEEE Trans. Instrum. Meas.*, vol. 56, no. 6, pp. 2284–2288, Dec. 2007.

[12] W. Zhang, S. B. Sohid, F. Wang, H. Cui, and B. Holzinger, “High-bandwidth combinational Rogowski coil for SiC MOSFET power module,” *IEEE Trans. Power Electron.*, vol. 37, no. 4, pp. 4397–4405, Apr. 2022.

[13] H. Li, Z. Xin, X. Li, J. Chen, P. C. Loh, and F. Blaabjerg, “Extended wide-bandwidth Rogowski current sensor with PCB coil and electronic characteristic shaper,” *IEEE Trans. Power Electron.*, vol. 36, no. 1, pp. 29–33, Jan. 2021.

[14] D. A. Weston, *Electromagnetic Compatibility: Principles and Applications*. New York, NY, USA: Marcel Dekker, 1992.

[15] R. Ludwig and G. Bogdanov., *RF Circuit Design: Theory and Applications*. Englewood Cliffs, NJ, USA: Prentice-Hall, 2010.

[16] TI, “OPA859 1.8 GHz unity-gain bandwidth, 3.3 nVHz, FET input amplifier,” 2018. [Online]. Available: https://www.ti.com/lit/ds/symlink/opa859.pdf